Fusion Engineering and Design 192 (2023) 113599

Contents lists available at ScienceDirect

Fusion Engineering and Design

journal homepage: www.elsevier.com/locate/fusengdes

Beam homogeneity of caesium seeded SPIDER using a direct beamlet current measurement

Alastair Shepherd [a,b,*], Tommaso Patton [b], Basile Pouradier Duteil [c,b], Antonio Pimazzoni [b], Andrea Rigoni Garola [b], Emanuele Sartori [d,b]

[a] Culham Centre for Fusion Energy (CCFE), Culham Science Centre, Abingdon, Oxfordshire, OX14 3DB, UK
[b] Consorzio RFX (CNR, ENEA, INFN, Università di Padova, Acciaierie Venete SpA), C.so Stati Uniti 4, 35127 Padova, Italy
[c] Ecole Polytechnique Fédérale de Lausanne (EPFL), Swiss Plasma Center (SPC), 1015 Lausanne, Switzerland
[d] Department of Management and Engineering, Università degli Studi di Padova, Strad. S. Nicola 3, 36100 Vicenza, Italy

ARTICLE INFO

Keywords:
SPIDER
Negative-ion source
Beam current
Beam optics
Beam uniformity

ABSTRACT

The ITER Heating Neutral Beam (HNB) source prototype SPIDER (Source for the Production of Ions of Deuterium Extracted from a Radio frequency plasma), hosted at the Neutral Beam Test Facility (NBTF) in Padova, Italy, has recently started operating with evaporated caesium in the source. This moves the primary H^- production mechanism from volume to surface processes, increasing the extracted H^- current while decreasing the co-extracted electron current. As in volume operation, the beam exhibits inhomogeneities across the vertical profile due to magnetic drifts, a result of the transverse filter field, which is vital for reducing the electron temperature near the extraction region. To minimise the occurrence of electrical discharges, SPIDER has been operated with a diminished number of extraction apertures to minimise the vessel pressure/ion source pressure ratio by means of a mask, which reduces the gas flow conductance between the source and the vessel. Therefore, it has been possible to directly measure the current of individual beamlets, due to the increased room between the beamlets, using the non-invasive Beamlet Current Monitor (BCM) diagnostic. Using measurements of five individual beamlets the homogeneity of the SPIDER H^- beam has been assessed, in a range of operating conditions with caesium in the source. The dependence of the beam homogeneity on source parameters (bias, filter field, RF power) has been observed, while increasing the Cs evaporation rate and unbalancing the power of the RF generators have proven to be effective at mitigating the beam inhomogeneity.

1. Introduction

For large magnetic confinement fusion devices with Neutral Beam Injection (NBI) systems, such as ITER, high-energy neutral beams are needed to effectively heat the plasma core. To reach up to 1 MeV of acceleration, negative ion beam sources are required, as positive ions have decreasing neutralisation efficiency over 100 keV. The ITER negative ion beam injector is undergoing testing and optimisation at the Neutral Beam Test Facility (NBTF) [1], hosted by Consorzio RFX (Padova, Italy), with two experiments: SPIDER and MITICA.

The latter is the full size ITER Heating Neutral Beam (HNB) prototype while SPIDER (Source for the Production of Ions of Deuterium Extracted from RF plasma) is the full-scale ITER ion source [2]. Using the tandem ion source concept, SPIDER has eight RF drivers, each with a diameter of approximately 275 mm. Each horizontal pair is connected to a 200 kW RF generator, to form the source plasma at a nominal filling pressure p_{fill} of 0.3 Pa.

To produce negative ions in sufficient quantities, a horizontal filter field is required to separate the hot plasma in the drivers from the colder plasma near the plasma grid (PG), which encloses the ion source. This is generated by a current running vertically through the PG, I_{PG}. In volume operation, this promotes the formation of vibrationally excited molecular hydrogen in the drivers, which expands towards the PG and undergoes dissociative attachment with cold electrons to form negative ions.

To increase the H^- production, caesium is evaporated into the source and redistributed by the plasma onto the PG, forming a low work function surface for the formation of H^- through surface processes [3]. The low electron temperature near the PG then reduces electron detachment, preserving the H^- availability for beam extraction.

Two electrostatic grids downstream of the PG, the extraction grid (EG) and grounded grid (GG), form the negative ion beam on SPIDER. The beam is composed of an 4 × 4 array of beamlet groups, with 80

* Corresponding author at: Culham Centre for Fusion Energy (CCFE), Culham Science Centre, Abingdon, Oxfordshire, OX14 3DB, UK.
E-mail address: alastair.shepherd@ukaea.uk (A. Shepherd).

https://doi.org/10.1016/j.fusengdes.2023.113599
Received 27 October 2022; Received in revised form 27 January 2023; Accepted 21 February 2023
Available online 2 March 2023

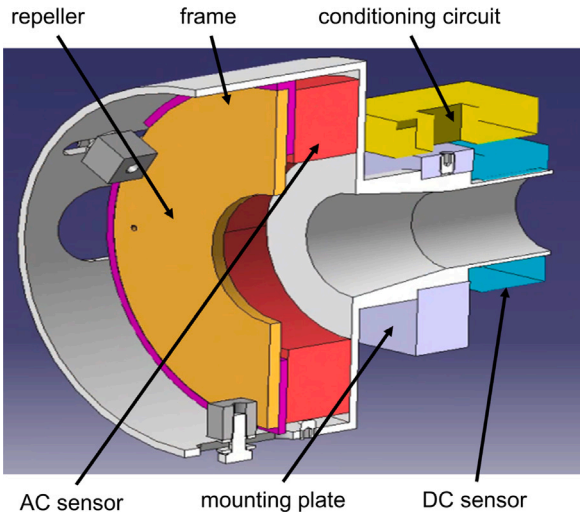

Fig. 1. BCM sensor module.

beamlets per group for a total of 1280 [4]. With the GG at ground potential the acceleration grid power supply (AGPS) and extraction grid power supply (ISEG) provide up to −96 kV acceleration voltage U_{acc} and −12 kV extraction voltage U_{ex} to the EG and PG respectively, so that the ion source can reach down to −108 kV.

Several source parameters have an impact on the homogeneity of the plasma, and consequently the beam. The power of the four RF generators can affect the distribution of the plasma, while the Cs dynamics influence the generation of H^- at the PG. Additionally, the presence of the filter field results in ExB and diamagnetic drifts in the source, creating a vertical plasma asymmetry [5,6]. Plasma electrodes in the extraction region, namely the plasma grid and bias plate (BP), can be biased to reduce the co-extracted electron current. This biasing influences the electric field and thus the drifts.

Vertical non-uniformities in the beam profile, and the interplay between the filter field and bias potential, have been observed in ITER-like negative ion beam sources on the beam segment scale [7]. On SPIDER, the uniformity of the accelerated beam has been studied on the beamlet scale, taking advantage of the reduced number of open PG apertures afforded by the PG mask [8]. Several SPIDER diagnostics can resolve the beam features on the beamlet scale, including the calorimeter STRIKE [9] and visible cameras. One recent diagnostic is the Beamlet Current Monitor (BCM) [10], which has measured the beamlet current for five beamlets during the Cs campaign.

The BCM beamlet current measurement is discussed in Section 2, with the measurements during SPIDER caesium operation presented in Section 3. The effect of the source parameters on the beamlet current homogeneity is discussed in Section 4 with two experimental methods of alleviating the vertical inhomogeneity given in Section 5.

2. Beamlet current monitor

The BCM is a series of five modules, each consisting of a DC sensor with conditioning circuit, an AC sensor and a repeller disk, to suppress backstreaming positive ions (Fig. 1). The modules are placed downstream of the GG to give the current measurement of five separate beamlets (Fig. 2). Each module is mounted to the PG mask support structure by a horizontal plate, which holds the sensor frame in line with the beamlet aperture.

The DC sensor is a LEM CSTR 0.3p closed loop fluxgate [11], with a custom conditioning circuit to reduce the sensor offset and increase the gain to around 250 V/A. Shepherd et al. have described the BCM DC sensor in more detail in an earlier paper [10], while the first analysis

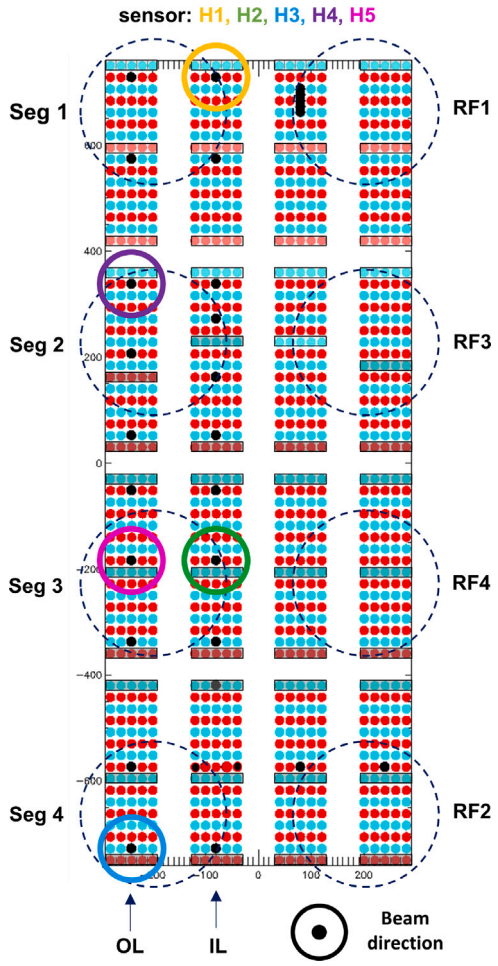

Fig. 2. Schematic of the GG, which is arranged in four rows of four beamlet groups (each row is a beam segment). Each group has 80 apertures, with the open apertures marked by filled black circles. The locations of the five beamlet current monitors are given by the coloured circles. Projections of the RF drivers (dashed circles) and the beamlets for the inner and outer left STRIKE tiles (IL and OL) are also indicated.

of the AC component of the beam is presented by Pouradier Duteil et al. [12].

During the 2021 campaign SPIDER was operated with so-called 'macro-pulses', long pulses of up to one hour made up of repeated short plasma phases, called 'blips', usually lasting less than one minute. The BCM is used for two different types of beam extraction (Fig. 3). The first has a constant extraction and acceleration voltage during a single plasma blip to allow a steady beam current for diagnostics that require averaging. The second is a ramp in extraction and acceleration voltage, keeping the voltage ratio constant, which allows the BCM to measure the Child–Langmuir curve of the beamlet in one plasma blip. In either case the sensor output voltage (black points) is filtered and the voltage baseline taken before and after beam extraction. This is due to the magnetic nature of the sensor making it sensitive to the filter field, which penetrates downstream of the PG, and to the plasma. By subtracting the voltage during steady RF power and I_{PG}, $V_{baseline}$, from the voltage during beam extraction $V_{beamlet}$ the voltage increase due to the beam passing through the sensor is calculated. Using the sensor gain G_s the beamlet current $I_{beamlet}$ is calculated (blue lines in Fig. 3b and d) using (1). In the example pulses shown, the beamlet current drops to a non-zero current at the end of the beam on phase because there is a short delay between the turn-off of the acceleration voltage U_{acc} the extraction voltage U_{ex}; some current is still measured due to extraction

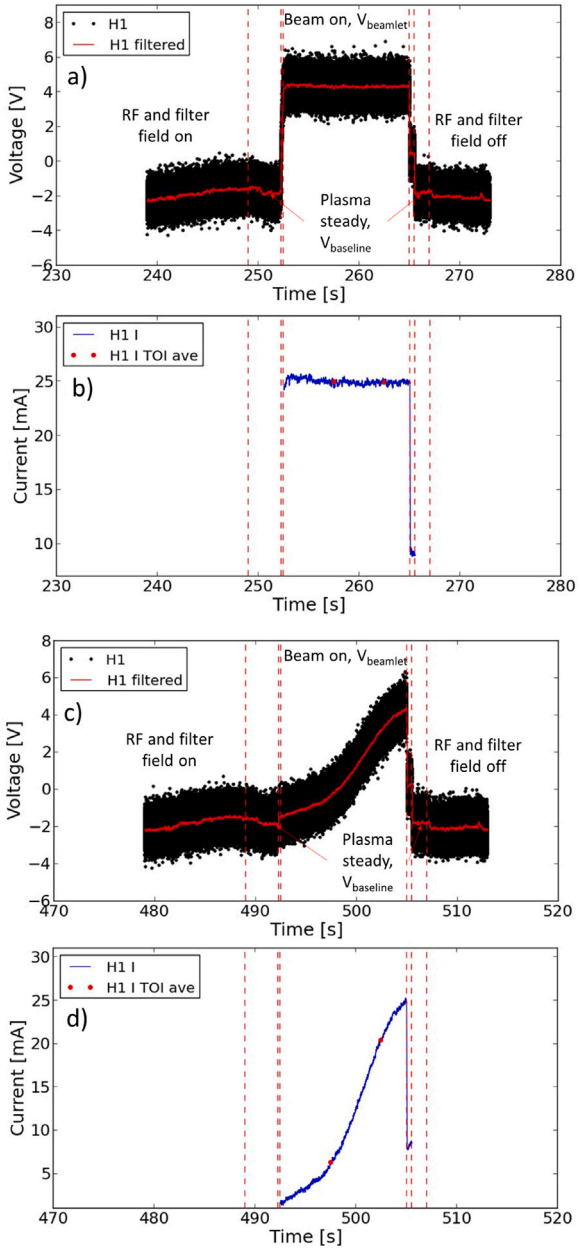

Fig. 3. Sensor H1 DC signal analysis for two plasma phases of pulse 9145. (a) and (c) Raw and filtered sensor voltage for constant and ramped beam voltage. (b) and (d) calculated beamlet current.

only, before the analysis ends with U_{ex}.

$$I_{beamlet} = V_{beamlet} - V_{baseline}/G_s \quad (1)$$

3. SPIDER Cs operation

The BCM operated continuously during the SPIDER Cs campaign, measuring the current of the five beamlets indicated in Fig. 2. The campaign is split into several operational phases, starting with Cs free operation (volume production of H^- only) before moving to the initial ceasiation of the source at 30 kW/driver. The average measured accelerated current density rises from 25 A/m^2 in pure hydrogen operation to 80 A/m^2 in Cs seeded operation (Fig. 4) after 12 pulses (blip 500), showing the effectiveness of the Cs layer in producing H^- ions. Note that the average current density measured by the accelerator power

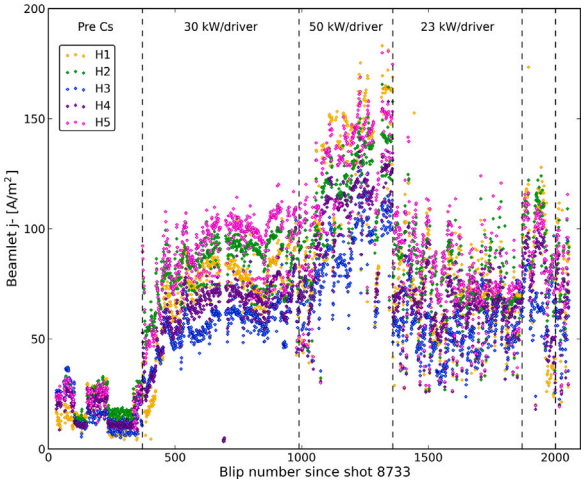

Fig. 4. Beamlet current measured by the BCM during SPIDER campaign S21 with Cs. Operational phases separated by dashed lines: Pre Cs (volume operation), Cs operation at 30 kW/driver, Cs operation at 50 kW/driver, parameter scans at 23 kW/driver. HV testing at 50 kW/driver and operation in deuterium in the final two phases.

supply was in general higher than the average current measured by the BCM. The differences are discussed in detail in ref [13].

During this phase, studies of the blip repetition rate and caesium injection rate were performed [14]. With the RF power increased to 50 kW/driver the average current increases to 140 A/m^2. Due to limitations on the acceleration grid voltage U_{acc} (50 kV), the best beam optical condition, with U_{acc}/U_{ex} around 10, could not be reached at high power as an extraction voltage U_{ex} greater than 7 kV is required to extract all of the available negative ions. Therefore, the RF power was decreased to 23 kW/driver to perform parameter scans investigating the beam optics and homogeneity with a lower negative ion density. Lastly, the RF power was returned to 50 kW/driver, to test for accelerator breakdowns when raising U_{acc}, followed by operation in deuterium gas instead of hydrogen. An increasing air leak resulted in a poorer caesium condition during the latter phases of the campaign.

The beamlets display a clear non-uniformity, both vertically and due to their positions within the beamlet group. Beamlet H1 (yellow), at the top of the source, is consistently higher than H3 (blue), located at the bottom of the source. In addition, beamlets H2 and H4 (green and pink) often have the highest current, due to them being located in the core of their respective beamlet groups.

The observed inhomogeneity is due to the varying availability of H^- for extraction across the source. A vertical non-uniformity in the negative ion density n_{H^-} near the PG has been previously determined in SPIDER using a combination of Langmuir probes, Optical Emission Spectroscopy and Cs Laser Absorption Spectroscopy [15]. The H^- distribution depends on the distributions of H^+ and e^- in the extraction region, as well as the distribution of the Cs layer on the PG. Therefore, the magnetic drifts that affect the plasma and Cs transport influence the distribution of H^- density, and thus the beam current.

4. Beam homogeneity

In Cs free operation, the STRIKE calorimeter has measured not only a general vertical non-uniformity but also inhomogeneities in the beam current at the beamlet group scale [16]. The latter manifests as a bell-shaped profile in the beamlet current, peaking in the centre of the beamlet group, and is believed to be due to the filter field reducing the diffusion of the plasma from the drivers. Similar behaviour has been observed by the BCM in Cs free operation. This paper assesses the inhomogeneity in the beamlet current using the BCM with surface production of H^- in a Cs seeded plasma. For the following pulses the Cs evaporation rate was 12 mg/h unless otherwise stated.

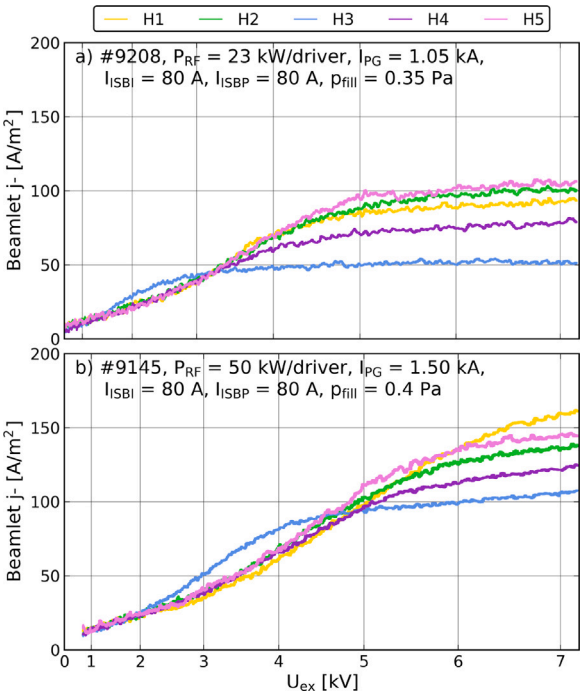

Fig. 5. BCM beamlet currents for extraction voltage scans at 23 kW/driver and 50 kW/driver. Current is plotted against $U_{ex}^{3/2}$, with the x-axis modified to show U_{ex}.

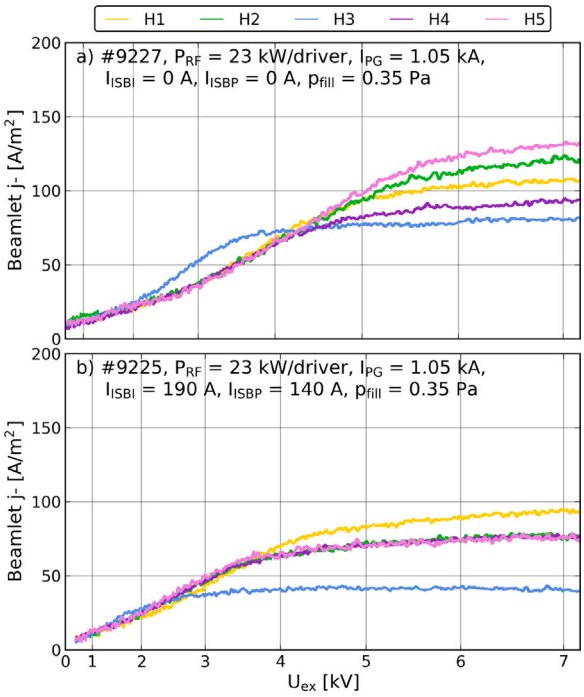

Fig. 6. BCM beamlet currents for extraction voltage scans at two different bias and bias plate currents. Current is plotted against $U_{ex}^{3/2}$, with the x-axis modified to show U_{ex}.

4.1. Extraction voltage

Before attempting to characterise the effect of the biasing and filter field on the beam homogeneity it is important to focus on the extraction voltage U_{ex}. Two examples of single blip extraction voltage scans (as in Fig. 3c), at two RF powers, are shown in Fig. 5. The current increases with U_{ex}, following the Child–Langmuir law, until no more H^- is available for extraction and the current saturates, while before saturation the beamlet currents are relatively homogeneous. The saturation current increases with RF power as the availability of H^- at the PG increases. After the knee, where the current deviates from Child–Langmuir, the inhomogeneity increases as the current reflects the distribution of the H^- availability in the source. In particular, the beamlet at the bottom of the source (H3) has a lower saturated current than the others. At lower extraction voltage the beamlets with higher H^- availability are not quite linear, believed to be caused by scraping on the EG due to higher perveance, while H3 has a larger current. When investigating source parameters care has to be taken to compare points at high U_{ex} so that all the available H^- is extracted.

4.2. Plasma grid and bias plate biasing

The PG and BP can be biased by separate power supplies — ISBI for the PG and ISBP for the BP — to reduce the co-extracted electron current. The biasing is controlled through the power supply output voltage $U_{ISBI/BP}$ or current $I_{ISBI/BP}$, with the latter method of control used during the experimental campaign. Scans of the bias and bias plate currents were performed at 23 kW/driver, to ensure that the extraction and acceleration voltages could be raised together. Six different combinations of I_{ISBP} [and I_{ISBI}] were investigated, 0 A [0 A, 80 A, 190 A] and 140 A [0 A, 80 A, 190 A], with U_{ex} scans for each. Two such scans are shown in Fig. 6.

At U_{ex} = 7 kV all of the beamlets are at saturation and a global decrease in beam current with bias current can be seen (Fig. 7). Normalising each beamlet by the maximum current (at zero bias), it is clear that the beamlet currents decrease proportional to their vertical position; the top beamlets decrease the least and the bottom beamlets the most. Experiments at BATMAN and simulations of single driver sources have proven that there is a vertical asymmetry in the plasma due to ExB drifts induced by the filter field [5,6,17]. Increasing the bias has been shown to increase the plasma asymmetry due to a strengthening of the Hall electric field as more electrons are drawn across the filter by the bias [18,19]. The increasing vertical non-uniformity in the SPIDER beamlet current with the bias can therefore be related to an increase in the source plasma asymmetry and a decrease in negative ion density at the bottom of the source. The biasing of the PG (I_{ISBI}) has a larger effect on the beamlet current than the bias plate (I_{ISBP}).

A similar effect can be seen in the IR calorimetric current measurement from STRIKE (Fig. 8), with the accelerated current decreasing by a factor of two between the top and bottom of the accelerator at high bias. Accompanying the decreased current is a higher divergence as the beamlets are increasingly away from perveance match: the negative ion current is too low for the set extraction voltage resulting in a larger beamlet divergence. It should be noted that the STRIKE measurements were taken at a lower extraction voltage than the BCM reached, as constant U_{ex} and U_{acc} are needed (as in Fig. 3b). From the U_{ex} scan in Fig. 6a it is clear that 4.94 kV is not high enough to reach saturation at low bias and the beamlets are near the knee of the Child–Langmuir curve where the distribution of beamlet intensities and widths (and thus divergence) are uniform. However, for showing the large top-bottom non-uniformity at high bias the data is suitable, as all of the available negative ions are extracted at 4.94 kV (Fig. 6b) and the decrease in beamlet current going from the top to the bottom of the source is comparable to the BCM.

With increased RF power (50 kW/driver) the effect of the bias on the beamlet current is still to increase the top-bottom inhomogeneity (Fig. 9). Looking at the drop in current density at the bottom of the source (H3), 30 A/m^2 at 50 kW/driver and 40 A/m^2 at 23 kW/driver, the magnitude of the decrease is comparable at the two RF powers. However, the relative size of the current drop going from low to high bias is lower at high power. The current density at the top beamlet (H1)

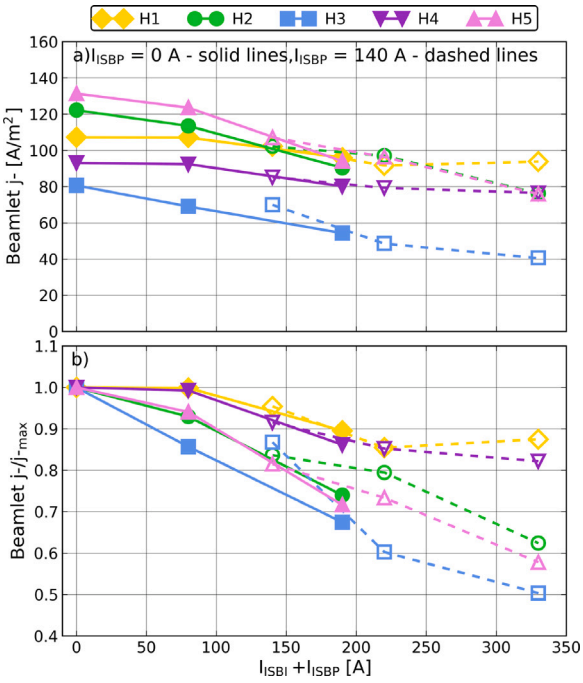

Fig. 7. (a) BCM beamlet current and b) beamlet current normalised to the individual beamlet maximum currents (at zero bias), for increasing total bias current (I_{ISBI}+I_{ISBP}). P_{RF} = 23 kW/driver, U_{ex} = 7 kV, I_{PG} = 1.05 kA, p_{fill} = 0.35 Pa.

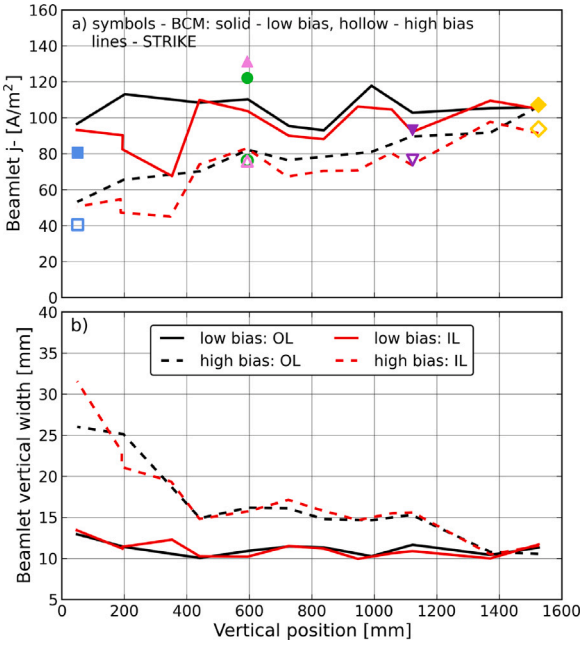

Fig. 8. (a) STRIKE current and (b) beamlet vertical width profiles on the inner (black) and outer (red) left tiles (looking to the source) for high and low bias cases from Fig. 7. P_{RF} = 23 kW/driver, U_{ex} = 4.94 kV, I_{PG} = 1.05 kA, p_{fill} = 0.35 Pa. Compared to BCM currents at 7 kV (coloured markers based on sensor location as in Fig. 2). Note that the inner column beamlets near 200 mm and 350 mm are at the edges of the beamlet group, nearest the bias plate, resulting in low current.

does not vary with bias. It is possible that the available current density at that position is higher, and that the applied extraction voltage of 7.5 kV was not enough to reach saturation (see Fig. 5b); therefore the beamlet current is constant, because it approaches the limit of the Child–Langmuir law rather than the limit of available negative ions.

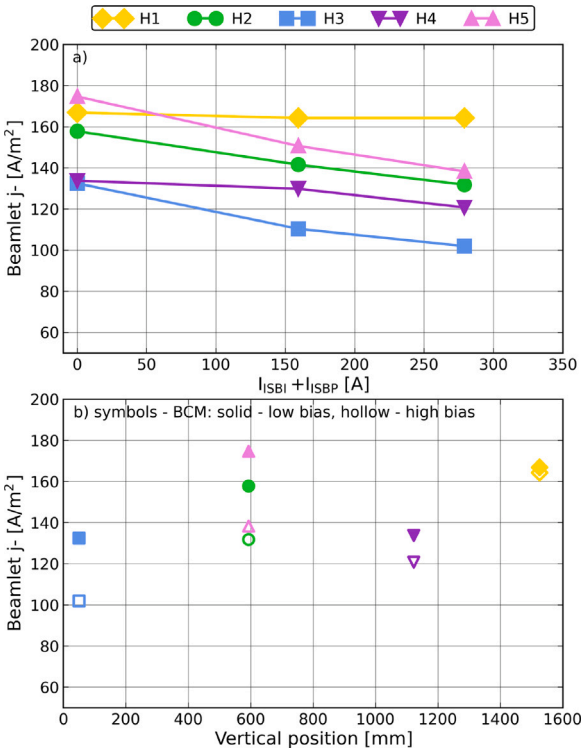

Fig. 9. (a) BCM beamlet current at high RF power (50 kW/driver) for increasing bias current. (b) BCM beamlet current vertical profile at low and high bias current. P_{RF} = 50 kW/driver, U_{ex} = 7.5 kV, I_{PG} = 1.5 kA, p_{fill} = 0.4 Pa.

4.3. Plasma grid current

Scans of U_{ex} were performed at fixed bias, varying the PG current from 0.9 kA to 1.2 kA (Fig. 10), corresponding to a peak field of 1.5 mT to 2 mT. The filter field decreases the current, with the edge beamlets (H1, H3, H4) decreasing more than the core beamlets (H2, H5). This is seen at high extraction voltage where all of the available H^- is extracted (Fig. 11a). Taking the vertical position of the beamlets relative to the centre of the nearest driver, a composite vertical profile of the beam for one beamlet group is obtained (Fig. 11b). With increasing filter field, the overall trend is a narrowing of the current profile across the group. Qualitatively this is comparable with the vertical current profiles measured on STRIKE in both volume [16] and surface operation (Fig. 12).

5. Improving homogeneity

The beam non-uniformity, in particular the top-bottom non-uniformity, is a direct consequence of non-uniformities in the plasma at the PG. This is seen in the spatially resolved source diagnostics, as described by Serianni et al. [15]. Steps taken to improve the plasma uniformity, and the H^- availability, should therefore be apparent in the beamlet current.

5.1. Cs flux

To improve the availability of H^- in the bottom of the source, which is lower in the bottom segment, the Cs evaporation rate was increased from 6 mg/h to 24 mg/h. This results in an increase in the beamlet current at the bottom of the source (Fig. 13, blue points for beamlet H3) as n_{H^-} increases. The other beamlets experience a smaller increase moving up the source. This may be due to U_{ex} not being high enough to

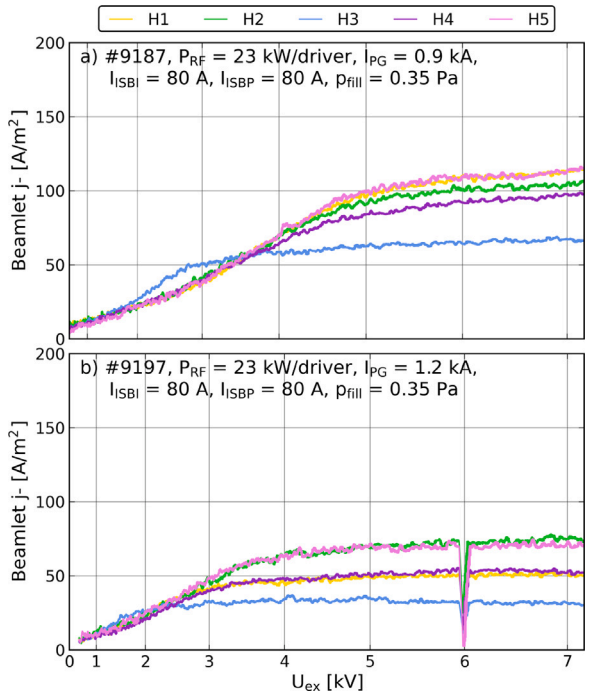

Fig. 10. BCM beamlet currents for extraction voltage scans at two different plasma grid currents. Current is plotted against $U_{ex}^{3/2}$, with the x-axis modified to show U_{ex}. A breakdown occurred during pulse 9197 at U_{ex} = 6 kV.

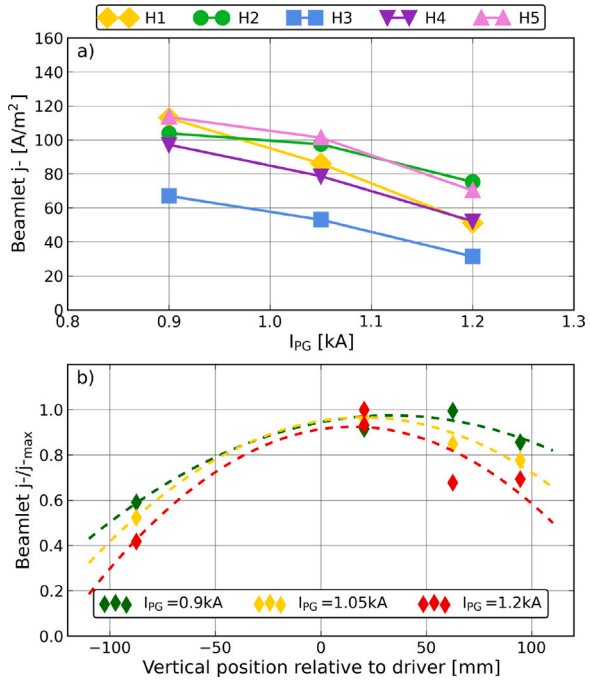

Fig. 11. (a) BCM beamlet current with increasing PG current and (b) normalised current against vertical position relative to nearest driver. P_{RF} = 23 kW/driver, U_{ex} = 7 kV, $I_{ISBI} = I_{ISBP}$ = 80 A, p_{fill} = 0.35 Pa.

fully extract all the available H⁻ at the top of the source, as discussed previously. However, estimates of n_{H^-} at the PG and BP have shown that at the top of the source n_{H^-} increases at the BP instead of the PG as the Cs flux is increased [15]. This implies that the H⁻ may move away from the PG into the expansion chamber instead of increasing further at the PG.

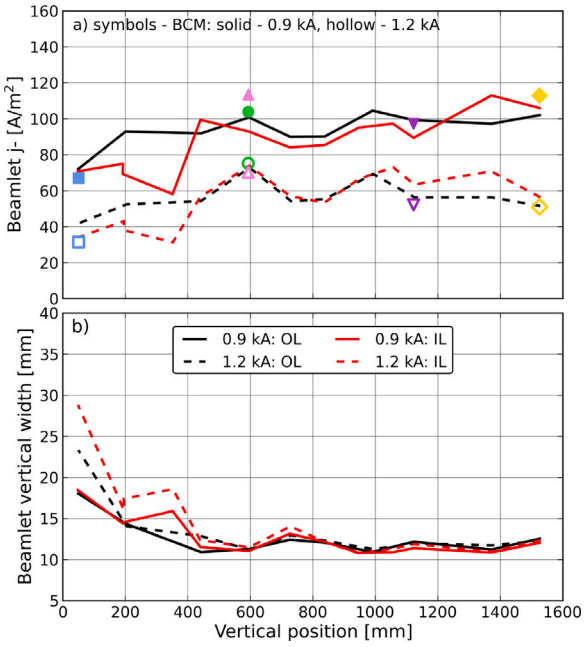

Fig. 12. (a) STRIKE current and (b) beamlet vertical width profiles on the inner (black) and outer (red) left tiles (looking to the source) for high and low PG current cases from Fig. 11. P_{RF} = 23 kW/driver, U_{ex} = 4.63 kV, $I_{ISBI} = I_{ISBP}$ = 80 A, p_{fill} = 0.35 Pa. Compared to BCM currents at 7 kV (coloured markers based on sensor location as in Fig. 2). Note that the inner column beamlets near 200 mm and 350 mm are at the edges of the beamlet group, nearest the bias plate, resulting in low current.

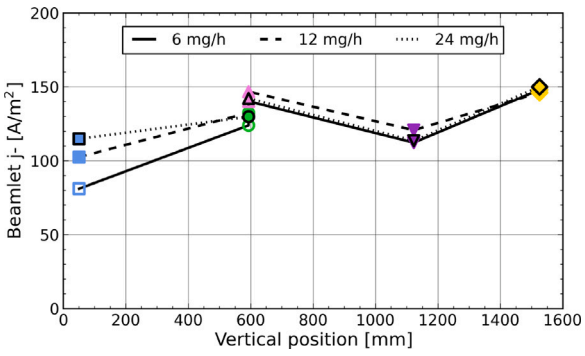

Fig. 13. BCM beamlet current vertical profile for different Cs fluxes. P_{RF} = 50 kW/driver, U_{ex} = 6.5 kV, U_{acc} = 45 kV, I_{PG} = 1.5 kA, $I_{ISBI} = I_{ISBP}$ = 80 A, p_{fill} = 0.35 Pa. Coloured markers based on sensor location as in Fig. 2.

5.2. RF power unbalancing

Increasing the H⁻ availability was also done by unbalancing the RF power of the generators, so that the segments with lower current would experience an increase in plasma density. Raising the RF power from 45 kW to 80 kW in the bottom segment results in a more homogeneous beamlet current distribution (Fig. 14).

6. Conclusion

Using the beamlet current monitors, a picture of the SPIDER beamlet current homogeneity has been obtained. Vertical top-bottom asymmetries in the plasma near the plasma grid, due to magnetic drifts, are reflected in the beamlet current. Increasing the bias increases the overall vertical non-uniformity. The cause of the drifts, the transverse filter field, also results in an inhomogeneity on the beamlet group scale, with higher currents at the centre of the beamlet groups. The

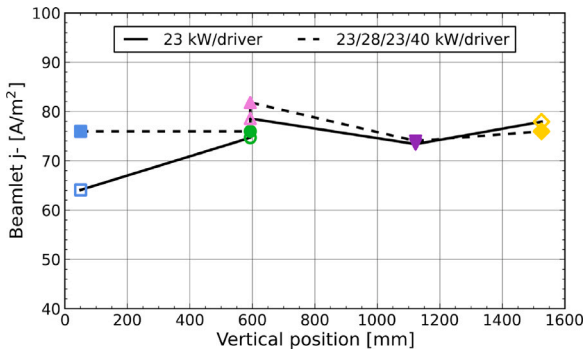

Fig. 14. BCM beamlet current vertical profile for equal and unequal driver RF powers. U_{ex} = 4.32 kV, U_{acc} = 42.4 kV, I_{PG} = 1.05 kA, I_{ISBI} = 80 A, I_{ISBP} = 0 A, p_{fill} = 0.35 Pa. Coloured markers based on sensor location as in Fig. 2.

inhomogeneites, both global and local to the beamlet groups, have been confirmed by STRIKE IR calorimetry.

Future operation of the SPIDER source with reduced apertures is planned, with solid-state RF amplifiers allowing 100 kW/driver and acceleration voltages greater than 60 kV. In an initial phase, the beam source could still be operated with a limited number of isolated beamlets. With that setup an enhanced number of DC beamlet current sensors, up to 15, will allow a more detailed study of beam current spatial uniformity.

Declaration of competing interest

The authors declare that they have no known competing financial interests or personal relationships that could have appeared to influence the work reported in this paper.

Data availability

Data will be made available on request.

Acknowledgements

This work has been carried out within the framework of the ITER-RFX Neutral Beam Testing Facility (NBTF) Agreement and has received funding from the ITER Organization. The views and opinions expressed herein do not necessarily reflect those of the ITER Organization.

This work has been carried out within the framework of the EUROfusion Consortium, funded by the European Union via the Euratom Research and Training Programme (Grant Agreement No. 101052200 — EUROfusion). Views and opinions expressed are however those of the author(s) only and do not necessarily reflect those of the European Union or the European Commission. Neither the European Union nor the European Commission can be held responsible for them.

This work was supported in part by the Swiss National Science Foundation, Switzerland.

References

[1] V. Toigo, R. Piovan, S.D. Bello, E. Gaio, A. Luchetta, R. Pasqualotto, P. Zaccaria, M. Bigi, G. Chitarin, D. Marcuzzi, N. Pomaro, G. Serianni, P. Agostinetti, M. Agostini, V. Antoni, D. Aprile, C. Baltador, M. Barbisan, M. Battistella, M. Boldrin, M. Brombin, M.D. Palma, A.D. Lorenzi, R. Delogu, M.D. Muri, F. Fellin, A. Ferro, A. Fiorentin, G. Gambetta, F. Gnesotto, L. Grando, P. Jain, A. Maistrello, G. Manduchi, N. Marconato, M. Moresco, E. Ocello, M. Pavei, S. Peruzzo, N. Pilan, A. Pimazzoni, M. Recchia, A. Rizzolo, G. Rostagni, E. Sartori, M. Siragusa, P. Sonato, A. Sottocornola, E. Spada, S. Spagnolo, M. Spolaore, C. Taliercio, M. Valente, P. Veltri, A. Zamengo, B. Zaniol, L. Zanotto, M. Zaupa, D. Boilson, J. Graceffa, L. Svensson, B. Schunke, H. Decamps, M. Urbani, M. Kushwah, J. Chareyre, M. Singh, T. Bonicelli, G. Agarici, A. Garbuglia, A. Masiello, F. Paolucci, M. Simon, L. Bailly-Maitre, E. Bragulat, G. Gomez, D. Gutierrez, G. Mico, J.-F. Moreno, V. Pilard, M. Kashiwagi, M. Hanada, H. Tobari, K. Watanabe, T. Maejima, A. Kojima, N. Umeda, H. Yamanaka, A. Chakraborty, U. Baruah, C. Rotti, H. Patel, M.V. Nagaraju, N.P. Singh, A. Patel, H. Dhola, B. Raval, U. Fantz, B. Heinemann, W. Kraus, S. Hanke, V. Hauer, S. Ochoa, P. Blatchford, B. Chuilon, Y. Xue, H.P.L.D. Esch, R. Hemsworth, G. Croci, G. Gorini, M. Rebai, A. Muraro, M. Tardocchi, M. Cavenago, M. D'Arienzo, S. Sandri, A. Tonti, The PRIMA Test Facility: SPIDER and MITICA test-beds for ITER neutral beam injectors, New J. Phys. 19 (8) (2017) 085004, [Online]. Available: http://dx.doi.org/10.1088/1367-2630/aa78e8.

[2] G. Serianni, V. Toigo, M. Bigi, M. Boldrin, G. Chitarin, S. Dal Bello, L. Grando, A. Luchetta, D. Marcuzzi, R. Pasqualotto, N. Pomaro, P. Zaccaria, L. Zanotto, P. Agostinetti, M. Agostini, V. Antoni, D. Aprile, M. Barbisan, M. Battistella, M. Brombin, R. Cavazzana, M. Dalla Palma, M. Dan, A. De Lorenzi, R. Delogu, M. De Muri, S. Denizeau, M. Fadone, F. Fellin, L. Ferbel, A. Ferro, E. Gaio, G. Gambetta, F. Gasparini, F. Gnesotto, P. Jain, A. Maistrello, G. Manduchi, S. Manfrin, G. Marchiori, N. Marconato, M. Moresco, T. Patton, M. Pavei, S. Peruzzo, N. Pilan, A. Pimazzoni, R. Piovan, C. Poggi, M. Recchia, A. Rizzolo, G. Rostagni, E. Sartori, M. Siragusa, P. Sonato, E. Spada, S. Spagnolo, M. Spolaore, C. Taliercio, P. Tinti, M. Ugoletti, M. Valente, A. Zamengo, B. Zaniol, M. Zaupa, C. Baltador, M. Cavenago, D. Boilson, C. Rotti, P. Veltri, T. Bonicelli, F. Paolucci, S. Muriel, A. Masiello, A. Chakraborty, H. Patel, N. Singh, U. Fantz, B. Heinemann, W. Kraus, M. Kashiwagi, K. Tsumori, SPIDER in the roadmap of the ITER neutral beams, Fusion Eng. Des. 146 (2019) 2539–2546, SI:SOFT-30. [Online]. Available: https://www.sciencedirect.com/science/article/pii/S0920379619305708.

[3] Y. Belchenko, G. Dimov, V. Dudnikov, A powerful injector of neutrals with a surface-plasma source of negative ions, Nucl. Fusion 14 (1) (1974) 113, [Online]. Available: http://dx.doi.org/10.1088/0029-5515/14/1/017.

[4] P. Agostinetti, V. Antoni, M. Cavenago, G. Chitarin, N. Marconato, D. Marcuzzi, N. Pilan, G. Serianni, P. Sonato, P. Veltri, P. Zaccaria, Physics and engineering design of the accelerator and electron dump for SPIDER, Nucl. Fusion 51 (6) (2011) 063004, [Online]. Available: http://dx.doi.org/10.1088/0029-5515/51/6/063004.

[5] L. Schiesko, P. McNeely, P. Franzen, U. Fantz, Magnetic field dependence of the plasma properties in a negative hydrogen ion source for fusion, Plasma Phys. Control. Fusion 54 (10) (2012) 105002, [Online]. Available: http://dx.doi.org/10.1088/0741-3335/54/10/105002.

[6] J.P. Boeuf, J. Claustre, B. Chaudhury, G. Fubiani, Physics of a magnetic filter for negative ion sources. II. E x B drift through the filter in a real geometry, Phys. Plasmas 19 (11) (2012) 113510, [Online]. Available: http://dx.doi.org/10.1063/1.4768804.

[7] F. Bonomo, I. Mario, D. Wünderlich, U. Fantz, On the vertical uniformity of an ITER-like large beam, Fusion Eng. Des. 159 (2020) 111760, [Online]. Available: https://www.sciencedirect.com/science/article/pii/S0920379620303082.

[8] M. Pavei, S. Dal Bello, G. Gambetta, A. Maistrello, D. Marcuzzi, A. Pimazzoni, E. Sartori, G. Serianni, F. Degli Agostini, L. Franchin, M. Tollin, SPIDER plasma grid masking for reducing gas conductance and pressure in the vacuum vessel, Fusion Eng. Des. 161 (2020) 112036, [Online]. Available: https://www.sciencedirect.com/science/article/pii/S0920379620305846.

[9] A. Pimazzoni, M. Brombin, G. Canocchi, R.S. Delogu, D. Fasolo, L. Franchin, B. Laterza, R. Pasqualotto, G. Serianni, M. Tollin, Assessment of the SPIDER beam features by diagnostic calorimetry and thermography, Rev. Sci. Instrum. 91 (3) (2020) 033301, [Online]. Available: https://doi.org/10.1063/1.5128562.

[10] A. Shepherd, B. Pouradier Duteil, T. Patton, A. Pimazzoni, A.R. Garola, E. Sartori, G. Serianni, Initial results from the SPIDER beamlet current diagnostic, IEEE Trans. Plasma Sci. (2022) 1–7, [Online]. Available: https://doi.org/10.1109/TPS.2022.3176757.

[11] Life Energy Motion, Current Transducer CTSR series datasheet. [Online]. Available: https://www.lem.com/sites/default/files/products_datasheets/ctsr_0_3-p_ctsr_0_6-p_v8.pdf.

[12] B. Pouradier-Duteil, A. Shepherd, T. Patton, A.R. Garola, R. Casagrande, First characterization of the SPIDER beam AC component with the beamlet current monitor, Fusion Eng. Des. 190 (2023) 113529, [Online]. Available: https://doi.org/10.1016/j.fusengdes.2023.113529.

[13] A. Shepherd, T. Patton, A. Pimazzoni, B.P. Duteil, A.R. Garola, E. Sartori, M. Ugoletti, G. Serianni, Direct current measurements of the SPIDER beam: a comparison to existing beam diagnostics, Contribution To the NIBS2022 Conference.

[14] E. Sartori, M. Agostini, M. Barbisan, M. Bigi, M. Boldrin, M. Brombin, R. Casagrande, S.D. Bello, M. Dan, B. Duteil, M. Fadone, L. Grando, A. Maistrello, M. Pavei, A. Pimazzoni, C. Poggi, A. Rizzolo, A. Shepherd, M. Ugoletti, P. Veltri, B. Zaniol, R. Agnello, P. Agostinetti, V. Antoni, D. Aprile, V. Candeloro, C. Cavallini, R. Cavazzana, M. Cavenago, G. Chitarin, S. Cristofaro, M.D. Palma, R. Delogu, M.D. Muri, S. Denizeau, F. Fellin, A. Ferro, C. Gasparrini, P. Jain, A. Luchetta, G. Manduchi, N. Marconato, D. Marcuzzi, I. Mario, R. Milazzo, R. Pasqualotto, T. Patton, N. Pilan, M. Recchia, A. Rigoni-Garola, B. Segalini, M. Siragusa, M. Spolaore, C. Taliercio, V. Toigo, R. Zagorski, L. Zanotto, M. Zaupa, M. Zuin, G. Serianni, First operations with caesium of the negative ion source SPIDER, Nucl. Fusion 62 (8) (2022) 086022, [Online]. Available: http://dx.doi.org/10.1088/1741-4326/ac715e.

[15] G. Serianni, E. Sartori, R. Agnello, P. Agostinetti, M. Agostini, M. Barbisan, M. Brombin, V. Candeloro, M. Dalla Palma, R. Delogu, M. De Muri, M. Fadone, I. Mario, T. Patton, A. Pimazzoni, C. Poggi, B. Pouradier-Duteil, B. Segalini, A. Shepherd, M. Spolaore, C. Taliercio, M. Ugoletti, P. Veltri, B. Zaniol, R. Pasqualotto, Spatially resolved diagnostics for optimization of large ion beam sources, Rev. Sci. Instrum. 93 (8) (2022) 081101, [Online]. Available: https://doi.org/10.1063/5.0084797.

[16] A. Pimazzoni, M. Agostini, M. Brombin, N. Marconato, E. Sartori, R. Pasqualotto, G. Serianni, Co-extracted electrons and beam inhomogeneity in the large negative ion source SPIDER, Fusion Eng. Des. 168 (2021) 112440, [Online]. Available: https://www.sciencedirect.com/science/article/pii/S0920379621002167.

[17] S. Lishev, L. Schiesko, D. Wünderlich, C. Wimmer, U. Fantz, Fluid-model analysis on discharge structuring in the RF-driven prototype ion-source for ITER NBI, Plasma Sources. Sci. Technol. 27 (12) (2018) 125008, [Online]. Available: http://dx.doi.org/10.1088/1361-6595/aaf536.

[18] C. Wimmer, U. Fantz, Dependence of the source performance on plasma parameters at the BATMAN test facility, AIP Conf. Proc. 1655 (1) (2015) 040004, [Online]. Available: https://aip.scitation.org/doi/abs/10.1063/1.4916446.

[19] G. Fubiani, J.P. Boeuf, Three-dimensional modeling of a negative ion source with a magnetic filter: impact of biasing the plasma electrode on the plasma asymmetry, Plasma Sources. Sci. Technol. 24 (5) (2015) 055001, [Online]. Available: http://dx.doi.org/10.1088/0963-0252/24/5/055001.